Journal of Petroleum Science and Engineering 183 (2019) 106433

Contents lists available at ScienceDirect

Journal of Petroleum Science and Engineering

journal homepage: www.elsevier.com/locate/petrol

Experimental study of fracture structure effects on acoustic logging data using a synthetic borehole model

Tianyang Li[a,b,c,*], Zizhen Wang[a,b,**], Yu Jeffrey Gu[c], Ruihe Wang[a,b], Yuzhong Wang[d]

[a] School of Petroleum Engineering, China University of Petroleum (East China), Qingdao 266580, PR China
[b] Key Laboratory of Unconventional Oil & Gas Development (China University of Petroleum (East China)), Ministry of Education, Qingdao 266580, PR China
[c] Department of Physics, University of Alberta, Edmonton, Canada
[d] No.2 Oil Production Plant Huabei Oilfield Company, PetroChina, Bazhou 065703, PR China

ARTICLE INFO

Keywords:
Fracture structure
Acoustic logging
Borehole model
Elastic moduli
Time and frequency analysis

ABSTRACT

Existing methods of well-logging interpretation often contain errors due to the presence of subsurface fracture networks within carbonate reservoirs. The differences of frequency ranges and measurement methods between the acoustic well-logging and indoor ultrasonic test cause inconsistent results. This study establishes a new method of devising a borehole model with controlled fracture structures, which is more suitable for large-scale experiments, such as borehole drilling and laboratory hydraulic fracturing. A self-build acoustic logging system is used to measure critically refracted waves in different directions and investigate the effects of fracture structures (porosity, aspect ratio-AR, and size) on the acoustic logging signals in the time and frequency domains using the Hilbert-Huang transform (HHT). Experimental results show that the velocity of the Stoneley wave is less sensitive to fracture structures than the velocity of the P- and S-waves, while strong effects are observed on the attenuation of the Stoneley wave. The best-fitting power and logarithmic functions are used to quantify the relationships between the properties (velocity and attenuation) and fracture structures. Predictions of the conventional rock-physical models used on high frequencies always overestimate the velocities at the well-logging scale. Intrinsic mode functions (IMFs) and marginal spectra show energy attenuation in different frequency ranges. Furthermore, fracture AR and size have similar mechanisms of scattering attenuation, which differ from the absorption attenuation of fracture porosity, and the effect of size is much stronger. The high precision of the borehole model has better implications than the rock-physical models for reservoir evaluations and predictions using acoustic logging or microseismic data at lower frequencies.

1. Introduction

Fractures are common geological features within the earth's crust, which control much of the transport properties of the rocks (Leary et al., 1990; Pan et al., 2018) and stress distribution around the wellbore (Meng et al., 2019). Complex morphology and structure of fractures in carbonate rocks are frequently documented, which are typically the byproduct of strong diagenesis and tectonism (Flügel, 2004; Mehrabi et al., 2016; Rahimpour-Bonab et al., 2012a) that have significantly impacted the porosity, permeability, and capacity of carbonate reservoirs (Choquette and Pray, 1970). Unfortunately, existing methods of well-logging interpretation ignore the effect of different fracture structures often resulting in multiple solutions in the evaluation of porosity in carbonate reservoirs as well as unrealistically low interpreted porosity within large production reservoirs (Li et al., 2018). On the other hand, fracture detection, such as microseismic logging in hydraulic fracturing operation (Li et al., 2019a), requires an accurate velocity model between seismic attributes and the physical properties of a given reservoir (Maxwell et al., 2010; Yuan et al., 2016). The study of acoustic wave propagation in unconventional reservoirs is a topic of great current interest.

Analysis of velocities and attenuation of the P-, S-, and Stoneley waves in acoustic logging interpretation, which can be detected from the original acoustic signals, is the practical method of estimating porosity and permeability (Asoodeh and Bagheripour, 2012; Li et al., 2019b; Rahimpour-Bonab et al., 2012b). At present, the ultrasonic pulse-transmission experiment is a conventional method to analyze the different fracture effects on rock acoustic properties (Amalokwu et al., 2016; Li et al., 2016). However, the ultrasonic test at the core scale is substantially different from the conventional acoustic logging method, which is mainly reflected in two aspects.

* Corresponding author. School of Petroleum Engineering, China University of Petroleum (East China), Qingdao 266580, PR China.
** Corresponding author. School of Petroleum Engineering, China University of Petroleum (East China), Qingdao 266580, PR China.
E-mail addresses: ltyupc@gmail.com (T. Li), wangzzh@upc.edu.cn (Z. Wang).

https://doi.org/10.1016/j.petrol.2019.106433
Received 6 May 2019; Received in revised form 12 July 2019; Accepted 26 August 2019
Available online 29 August 2019
0920-4105/

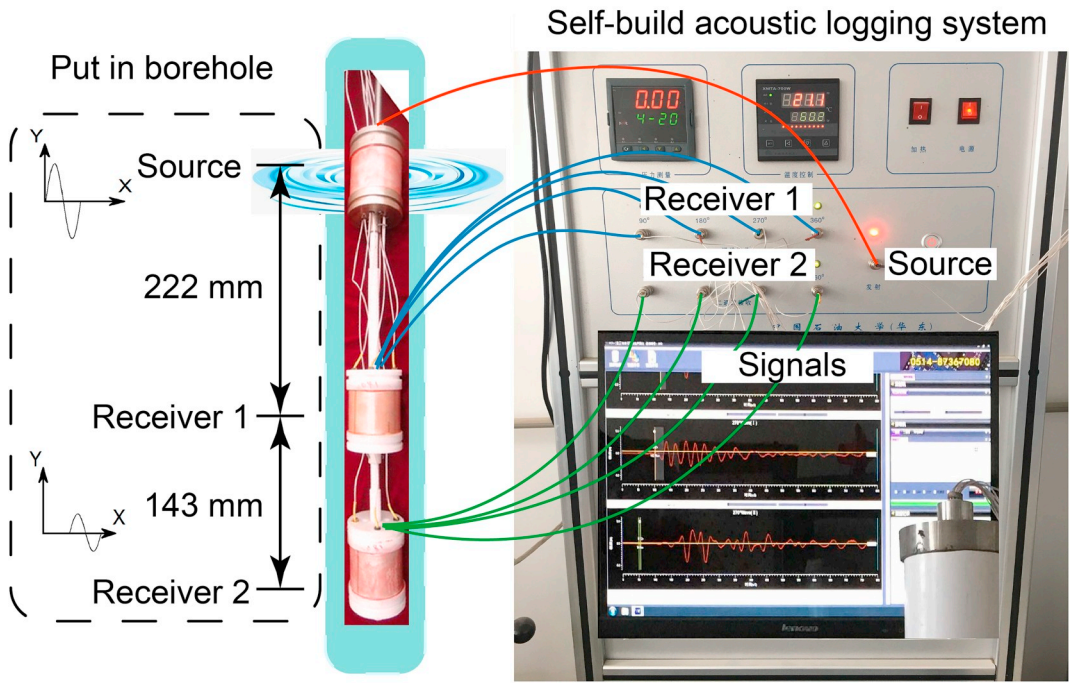

Fig. 1. The self-build acoustic logging system with one ring-emitting piezoelectric source (upper) and two piezoelectric receivers (lower). The source-receiver distances are 222 mm and 365 mm for the two receivers.

First, compared with the transmission measurement of the ultrasonic test, acoustic logging aims to measure the critically refracted waves in the formation. This approach is error-prone since the recorded wave during acoustic logging contains not only the direct P- and S-waves, but also an extensive series of guided waves, such as Stoneley and pseudo-Rayleigh waves (Spies, 1996; Tang and Cheng, 1993). Second, crustal rocks exhibit different physical properties with different elastic wave frequencies (Hornby et al., 1989; Jeppson and Tobin, 2015). The frequency of conventional acoustic logging is approximately 10–50 kHz, while by contrast, the laboratory core scale is smaller, and the frequency of the ultrasonic test is significantly higher (~1 MHz). Consequently, a direct application of an ultrasonic test will cause errors in the acoustic logging interpretation.

Building rock physical models with known fracture structures is the primary method to quantitatively investigate the fracture structure effects on velocity and attenuation (Shuai et al., 2018). For complex fracture structures, the distribution and shape of the fractures in three-dimensional space are random, which present a significant challenge to computed tomography (CT) or scanning electron microscope (SEM) to obtain a numerical model (Liu et al., 2016) – a major limitation of these methods (i.e., small-scale and high cost) at logging scales (0.1–10 m). The technology of artificial sandstone core has become relatively mature. In general, the matrix is made by sandstone grains cemented with epoxy resin and materials to simulate the fractures such as plexiglass, epoxy, aluminum, copper, and tinfoil sheets (De Figueiredo et al., 2013; Zhu et al., 2016). However, existing methods generally adopt epoxy resin as the cementing agent, though high consistency and cost limit its application to the production of small-scale cores rather than borehole models at larger scales. A new method to develop a borehole model with controlled fracture structures, an improvement over existing approaches for simulating acoustic logging in carbonate reservoirs, was reported in this paper. A self-build acoustic logging system was used to measure the critically refracted waves in different directions to investigate the effects of fracture structures on acoustic logging data in time and frequency domains using the Hilbert-Huang transform (HHT). This work aims to build a foundation for fracture identification based on elastic wave data, such as acoustic logging and microseismicity, which can enhance fractured-reservoir exploration and development efficiency of carbonate rocks.

2. Experimental procedures

Three criteria for designing a borehole model are imposed. First, the matrix must exhibit homogenous and stable properties that allow appropriate comparisons with actual carbonate rocks. Second, the distribution of the fractures in the model must be controlled to minimize the effect of fracture angles (Guo et al., 2018). Third, this model must be a proxy for practical acoustic logging to bridge experimental syntheses and field observations effectively. With the above criteria in mind, an 800 mm deep, 315 mm wide concrete model with different fracture structures is designed. This model is pierced along its axis by a 76 mm wide borehole filled with water. A self-build acoustic logging system, with one ring-emitting piezoelectric source and two receivers, was used to explore the effect of fracture structures on acoustic logging observations.

2.1. Acoustic measurement system

Piezoelectric-ceramic transducer can convert electrical signals into pressure signals (source), and conversely, convert pressure signals into electrical signals (receiver). A self-build acoustic logging system is built with one ring-emitting piezoelectric source and two piezoelectric receivers (as shown in Fig. 1). The diameter of the transducer is less than 55 mm. Each receiver consists of four piezoelectric ceramics with an angle difference of 90°. Together, four waveforms can be retrieved for each model, which makes the experiment results more reliable. The dominant frequency of the acoustic logging system is 20–40 kHz. For each measurement, the received signal is recorded at a sampling rate of 10 MHz with a length of 400 μs and repeated 100 times to minimize fluctuation errors.

2.2. Matrix design

As a commonly used building material, cement has been widely used in drilling engineering with the advantages of having low cost, high strength, easy accessibility, known mechanical behavior, and the simplicity to mold to different sizes (Du et al., 2019; Sarmadivaleh and Rasouli, 2014). During the wait on cement (WOC), the compaction effect is not a significant factor in its final property. These properties are suitable for producing large-scale models in hydraulic-fracturing

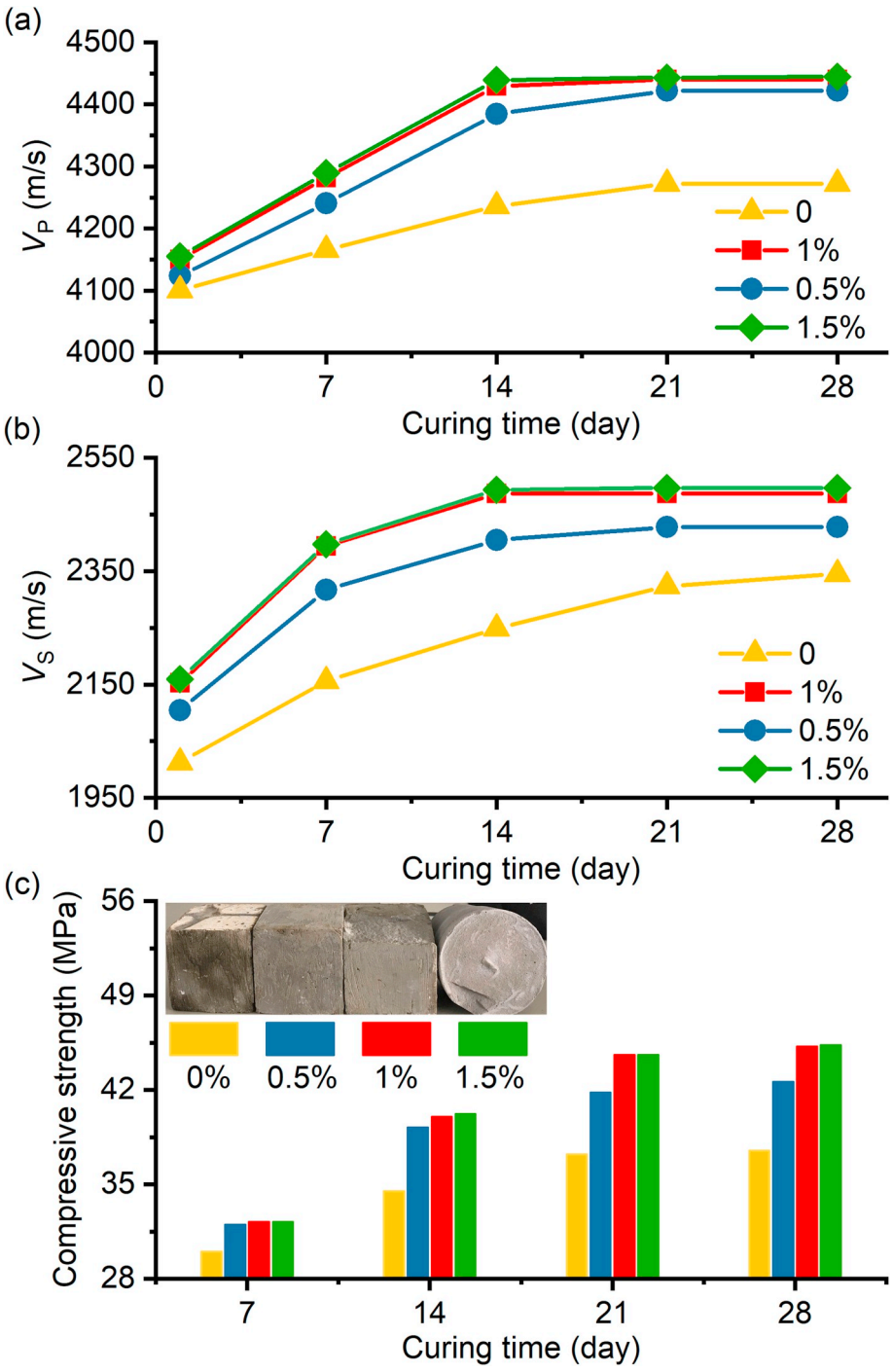

Fig. 2. Plot of different micro-silicon additions on the physical properties of the matrix under normal temperatures and dry conditions. The (a) P-wave velocity, (b) S-wave velocity, and (c) compressive strengths were measured after curing for 1, 7, 14, 21, and 28 days.

experiments (Crampin et al., 2015; Zhou et al., 2010). On the other hand, the low density, short sedimentation time, and tendency to produce bubbles from a pure cement system cause undesired effects on elastic wave propagation through the borehole model. In this study, a consolidated mixture of natural carbonate cuttings and cement slurry is used to simulate a carbonate reservoir.

The cement properties (density and strength) are determined by the grain composition with the different ratios of cement and other mixed materials (Haach et al., 2011). To simulate the actual carbonate formations (well consolidation and low primary porosity) using physical models, we choose cement, carbonate cuttings, and micro-silicon with different grain sizes as the solid-phase. Adding micro-silicon can effectively avoid the sedimentation during WOC to eliminate the density difference between the upper and lower layers when the model is relatively large. The Class-G oil well cement is produced by Shandong ShengWei Enterprise Company. The carbonate cuttings are clean crystalline grains with a grain size of 150 μm, and the SiO_2 content of the micro-silicon powder is greater than 97%.

Micro-silicon with grain sizes less than a micron has modest influences on the physical properties of the matrix, but can substantially improve the overall thixotropy of the system. The result of the correlations (Fig. 2) shows the influence of different micro-silicon additions on the physical properties of the matrix under normal temperatures and dry conditions. The mass ratio of carbonate cuttings, cement, and water

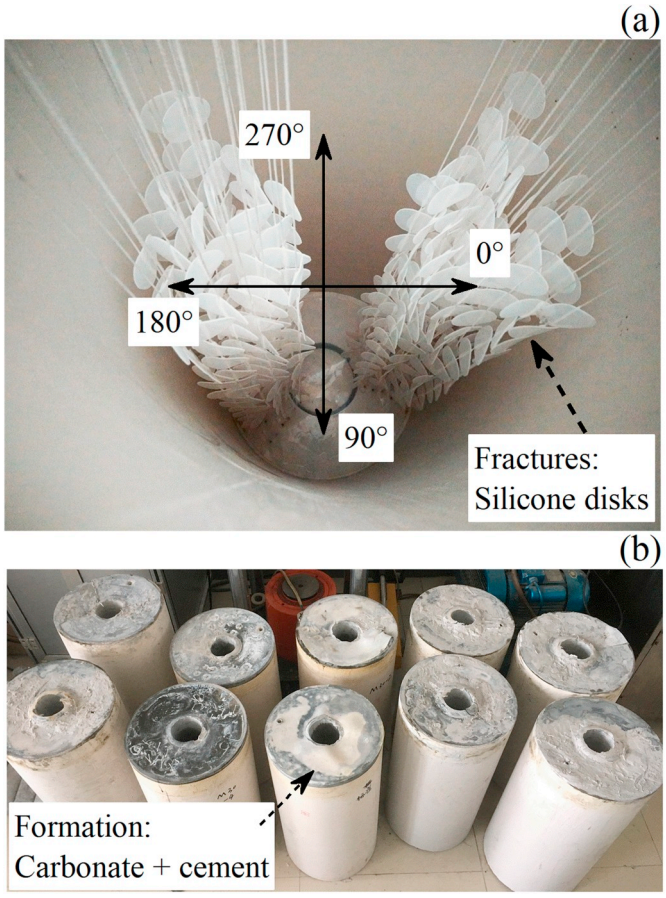

Fig. 3. Physical models with a vertically aligned fracture system. (a) The distribution of the silicone disks. (b) Synthetic borehole models were held for 21 days.

is 1: 1: 0.4. To discharge the bubbles formed during agitation, we add 0.1% graft polymers of sulfonated aldehyde-ketone condensation as the drag reducer and 0.2% polymers of polyether and organic silicon as the defoamer. When the mass ratio of micro-silicon exceeds 1%, the overall physical properties stabilize after 21 days, which is conducive to the final performance. Considering the structure and physical properties, the mass radio of micro-silicon is chosen to be 1%. After several tests, the preparation method of the borehole model with controlled fracture structures is obtained, which is more similar to the actual reservoir rocks than the simple cement system.

2.3. Fracture design

Fractures in actual carbonate rocks usually exhibit irregular shapes (Weger et al., 2009), which makes it challenging to build rock-physical models with known fracture structures. Most of the theoretical or laboratory models simplify the different fracture shapes by regular spherical or ellipsoidal inclusions, while assuming an aspect ratio (AR; the ratio of the minor axis to the major axis) and size of inclusions to account for the effect of fracture structures on the elastic properties of the carbonate rocks (Blum et al., 2011; Tillotson et al., 2012). Due to apparent differences in the physical properties between pore fluids and carbonate rocks, silicone material, which is similar to fluids with relatively low density compared with the above matrix, is chose as the filling material. Penny-shaped silicone disks with different thicknesses and diameters are used to simulate the fractures, which can easily achieve single variable control. In the horizontally layered sedimentary strata, rock fractures are mostly distributed vertically (Crampin et al., 2015) due to the orientation of the maximum vertical stress. Hence, the experimental design of the borehole model is to simulate the vertical fractures distributed in a carbonate formation.

Due to the low strength and density of the silicone disks in the flow matrix, a soft line is adopted to connect the silicone disks and then straightened after the injection of the cement slurry to control the orientation of fraction distribution. The cylindrical mold is divided into four parts (every 90°), and the silicone disks are evenly distributed in the borehole model (Fig. 3a). In the model, the fractures are distributed in 0° and 180° directions, whereas the vertical directions (90° and 270° directions) contain no fractures. We first mixed 50 kg of cement and 20 kg of water, and then gradually added 75 kg of carbonate cuttings and 1.25 kg of micro-silicon. The masses of drag reducer and defoamer are 125 g and 250 g, respectively. Subsequently, we poured the mixture into the cylindrical mold and immersed a concrete shaker into the slurry and operated for 1 min to discharge the bubbles. The models were held for 7 days at normal temperature for the mixture to cure. A vertical well hole of 76 mm width and 600 mm depth was drilled into the center of the model and filled with water to simulate the petroleum drilling procedure (Fig. 3b). After 21 days, the cement hydration was fully completed, and a synthetic borehole model was obtained.

Finally, three sets of low-porosity borehole models with different fracture structures were built to analyze the effects of fracture porosity, AR, and size on acoustic logging signals according to the control variable method. The porosity (ϕ) of the model can be obtained as:

$$\phi = \frac{2Nd^2h}{(D_f^2 - D_w^2)L_y} \tag{1}$$

where N is the total number of fractures in each model, d and h are the diameter and thickness of the fractures, respectively. D_f and D_w are the respective outer and inner diameters of the borehole model, and L_y is the height of the borehole model.

2.4. Acoustic processing

The self-build source and receivers are placed in the borehole model that filled with water as Fig. 4 shows. The typical waveforms received in the measurements are shown in Fig. 5. The acoustic time of the model is calculated by two receivers in the same direction. The elastic-wave velocity in the borehole model is calculated:

$$V_i = \frac{\Delta l}{t_{2i} - t_{1i}} \tag{2}$$

where V_i is the velocity of ith phases (P-, S- and Stoneley waves) in km/s, Δl is the length between the two receivers in mm, while t_{1i} and t_{2i} are the picked ith arrival times of all phases waves of the two received signals in μs.

The measured velocities can be used to calculate the dynamic module by (Schmitt, 2015):

$$K = \rho_b\left(V_p^2 - \frac{4}{3}V_S^2\right) \tag{3}$$

$$\mu = \rho_b V_S^2 \tag{4}$$

where K and μ are the dynamic bulk and shear moduli, respectively, in units of GPa, ρ_b is the bulk density of the borehole model in g/cm^3, and V_P and V_S are the respective P- and S-wave velocities in km/s.

The effects of fractures with different structures are evident in both time and frequency domains. The acoustic signals are generally nonlinear and nonstationary with multiple frequencies (Li, 2003). The HHT is used to analyze the frequency characteristics of the waveform, which is an effective method to decompose a signal into 'intrinsic mode functions' (IMFs) along a trend to obtain instantaneous frequency data (Huang et al., 2008); this approach has been used extensively in signal processing (Fan et al., 2017). This transform is performed using two main steps (Appendix A). First, IMFs are extracted from the signal based on empirical mode decomposition (EMD), in view that the first four IMF

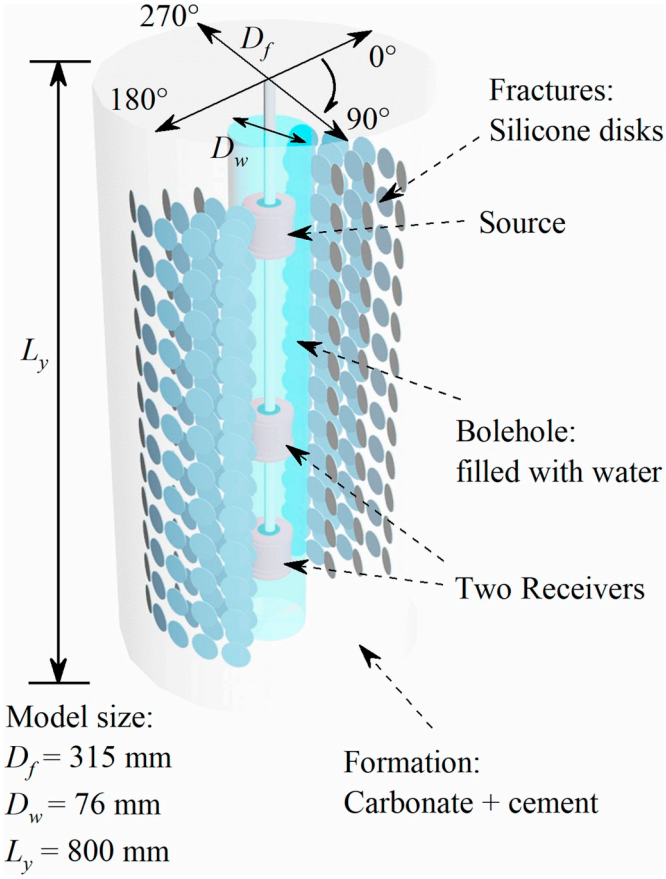

Fig. 4. A 3-D physical model with the self-build acoustic logging system.

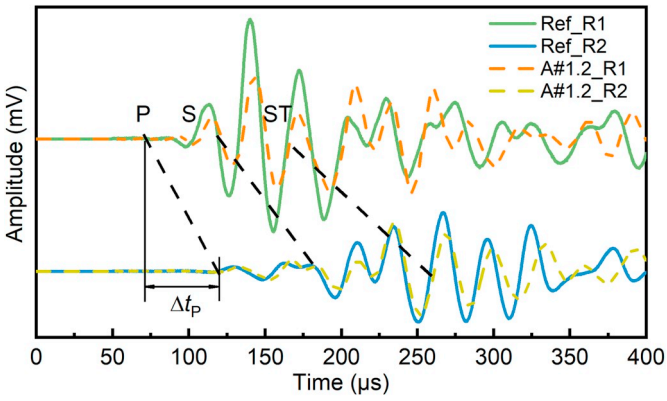

Fig. 5. Typical waveforms from the reference model without fractures and the A#1.2 model. The differential times of the three phases (P-, S-, and Stoneley waves) between the two receivers (R1 and R2) are used to calculate the wave velocities.

Table 1
Deviation of physical properties with different measurement methods.

Methods	V_P (km/s)	V_S (km/s)	K (GPa)	μ (GPa)
Ultrasonic	4.51	2.62	23.83	14.62
Acoustic logging	4.19	2.42	20.76	12.47
Deviation (%)	7.6	8.3	14.8	17.2

components (IMF1-4) contain the most substantial amount of information (Bowman and Lees, 2013). Second, the Hilbert transform (hereafter, $H(\omega, t)$) is applied to each IMF component to obtain the instantaneous frequency and energy distribution. Then, $H(\omega, t)$ is integrated over the entire time domain to calculate the marginal spectrum $h(\omega)$, which is the sum of the total magnitude for each frequency.

Table 2
Model sets and the corresponding parameters.

Sets	Models	N	h (mm)	d (mm)	AR	ϕ (%)
A	A#0.6	6 × 24	1	30	0.033	0.6
	A#1.2	12 × 24	1			1.2
	A#1.8	12 × 36	1			1.8
	A#2.4	12 × 48	1			2.4
	A#3.0	12 × 60	1			3.0
B	B#0.017	12 × 48	0.5	30	0.017	1.2
	B#0.033	12 × 24	1		0.033	
	B#0.067	12 × 12	2		0.067	
	B#0.13	6 × 12	4		0.13	
C	C#10	24 × 216	0.5	10	0.05	1.2
	C#20	12 × 54	1	20		
	C#30	12 × 16	1.5	30		
	C#40	6 × 14	2	40		
	C#50	6 × 7	2.5	50		

3. Results and discussion

After WOC for 30 days, the V_P and V_S of the modeled borehole matrix without fractures were measured by the ultrasonic transmission test (central frequency = 500 kHz) as well as the acoustic logging system (central frequency = 40 kHz). The results are tabulated in Table 1. The deviations of V_P and V_S of the same model can be obtained by the different measurements. In particular, the physical properties measured by the ultrasonic test are significantly higher than those by the acoustic logging method. The shear modulus (μ) shows higher deviations than the bulk modulus (K).

In the long-wavelength limit, the elastic response of fractured rock is described by equivalent-medium theories (EMT). These models accurately predict frequency-independent behaviors and, to a significant degree, conform to EMT. Hence, we analyze the effects of fracture porosity, AR, and size in the following sections and compare with those of EMT (long-wavelength limit) and ray (short-wavelength limit) (Kuster and Toksöz, 1974) models to gain further insight into the phenomena that control elastic wave propagation in the borehole models. The parameters of the model sets A, B, and C describing the fracture geometry are listed in Table 2. For each model set, a blank model without fractures is prepared by the same process for comparison.

3.1. Effect of fracture porosity

Fracture porosity is the primary parameter of the reservoir, which significantly affects the propagation of waves (Shalaby and Islam, 2017). The borehole models of set A have the same fracture size (d = 30 mm) and AR (AR = 0.033) but different fracture porosities (ϕ = 0%–3%). The measurements from the model set A are analyzed to investigate the effects of fracture porosity on the velocity and attenuation of all phases in time and frequency domains.

The cross-plot between the velocities of three phases and porosity (Fig. 6) shows that the velocities in two directions (0° and 180°) are relatively consistent, indicating that the borehole models are stable and repeatable enough to offer reliability for the subsequent data analysis. As the fracture porosity increases from 0 to 3%, the Stoneley wave velocity (V_{ST}) does not show a noticeable decrease, whereas the V_S and V_P drop off more significantly. The velocities and porosities are negatively correlated, a relationship that has been verified earlier through rock-physical experiments (Han et al., 1986). The slope of V_P is larger than that of V_S, suggesting that bulk modulus is more sensitive to porosity than the shear modulus. The overall degree of variation is

small, however, especially in V_S and V_{ST}. To investigate further, we use conventional rock-physical EMT of KT model (Kuster and Toksöz, 1974) and DEM model (Berryman, 1992), which vary with elastic moduli, porosity, and AR. The results show that the time-average model (Cerveny and Brown, 2003) used in seismic exploration provides comparatively higher V_P and V_S at the same porosity. The parameters used in these theoretical models are the same as those of the borehole model, which are evident from the equal velocities when $\phi = 0\%$. The theoretical models always overestimate V_P and V_S, and the deviations become larger as porosity increases. The predictions of KT and DEM models are similar to each other, and the DEM models have closer outcomes to the experiments.

Wave attenuation in rocks, which is exponential with its propagation distance in general, is more complicated than velocity according to earlier studies (Johnston et al., 1979; Kuster and Toksöz, 1974), due to its dependencies on porosity and different properties between rocks and fractures. Also affected is the Stoneley wave, a wave group that propagates along with the solid-fluid interface and is sensitive to fractures (Tang and Cheng, 1993). The cross-plot of amplitudes of the three wave phases with different porosities (Fig. 7) shows that the amplitude of the Stoneley wave is more severely influenced by porosity than P- and S-waves. The attenuation of the Stoneley wave amplitude reaches 83.3%

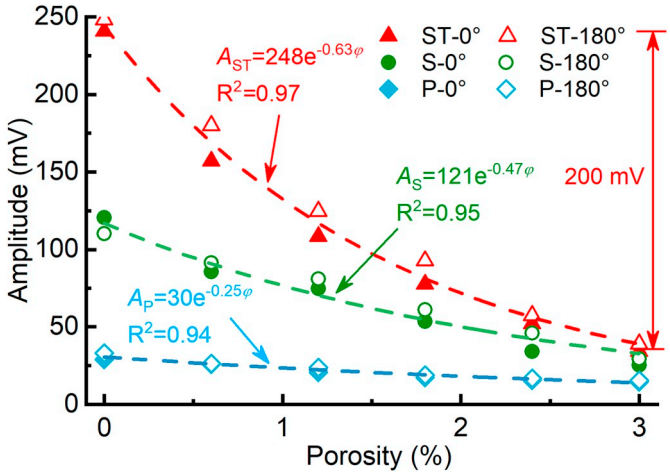

Fig. 7. Relationship between fracture porosity and amplitudes of P-, S-, and Stoneley waves. The term of determinant coefficients (R^2) of the exponential function shows large amplitude drop-offs in Stoneley waves. The color conventions are the same as those in Fig. 6. (For interpretation of the references to color in this figure legend, the reader is referred to the Web version of this article.)

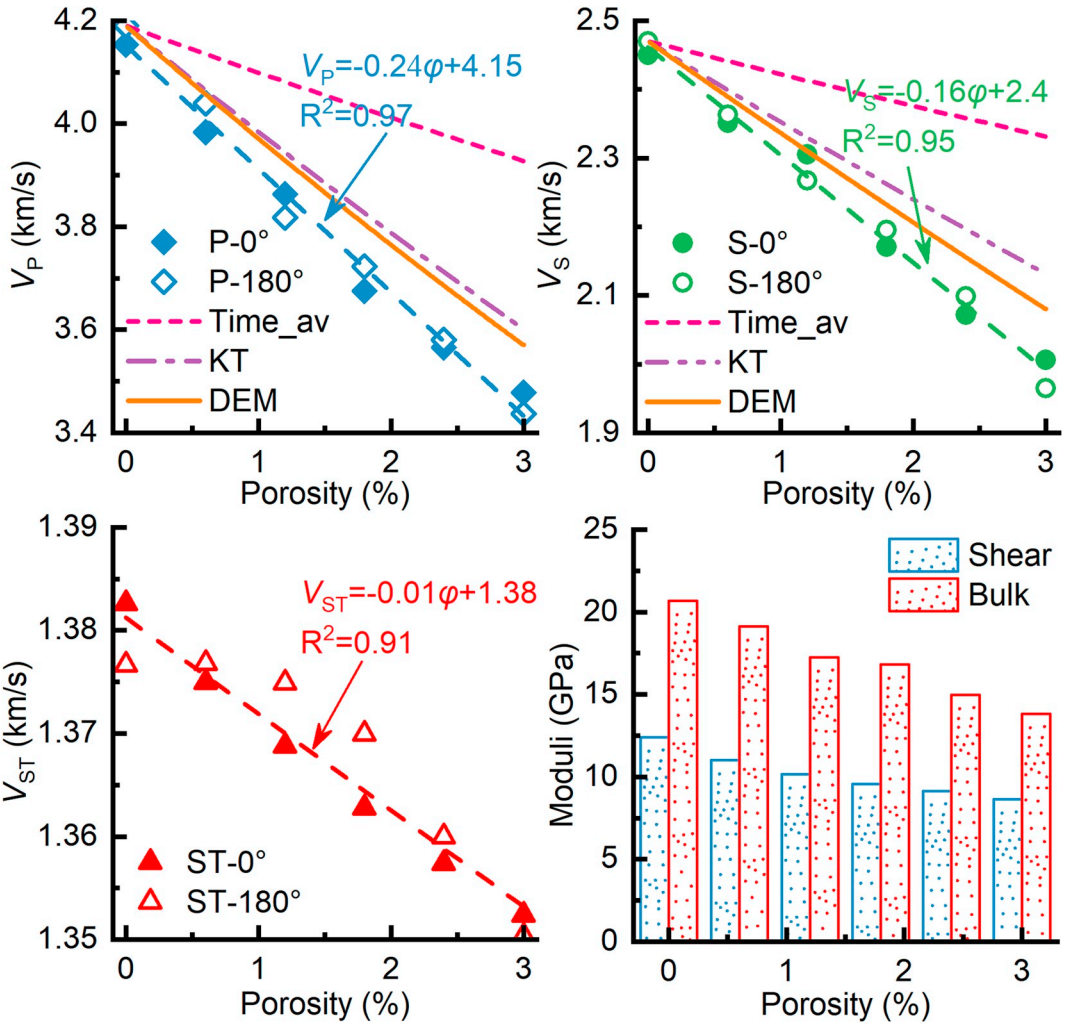

Fig. 6. Influence of porosity on the velocities and elastic moduli for the model set A. Solid and unfilled symbols represent the results measured in 0° and 180° directions, respectively. The corresponding lines are the best-fit linear functions for the velocities of each wave phase. The dashed red line corresponds to the data sets combined with solid and unfilled triangles. The dashed green line corresponds to the data sets combined with solid and unfilled circles. The dashed blue line corresponds to the data sets combined with solid and unfilled diamonds. The fracture AR (AR = 0.033), size (d = 30 mm), and source frequency in these models are constant. The determinant coefficient (R-squared value) denotes the determinant coefficient of the best-fit function. Two EMT models (KT and DEM) and the time average model are used to compare with the experimental results. (For interpretation of the references to color in this figure legend, the reader is referred to the Web version of this article.)

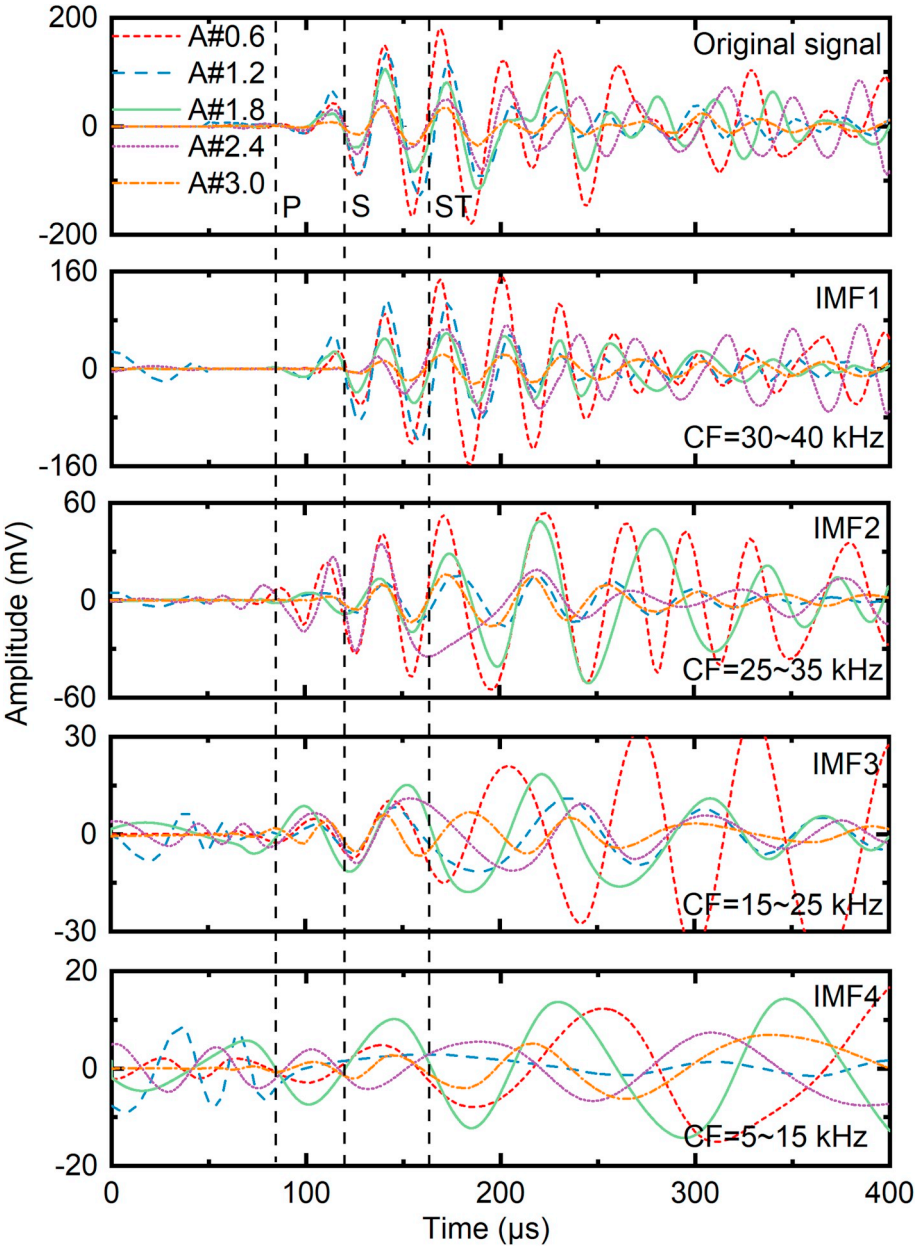

Fig. 8. The original signals received by R1 and the corresponding IMF components of the model set A. The CF of each IMF component is computed by the FFT. The first arrivals of P-, S-, and Stoneley waves in A#3.0 model are labeled by the vertical dash lines by picking the first breaks of each wave phase.

(decreases from 240 mV to 40 mV) but only 73.9% for the S-wave (drops from 115 mV to 30 mV) and 51.6% for the P wave (drops from 31 mV to 15 mV).

Much of the attenuation could be attributed to the presence of fractures, which causes frequency-dependent changes to the transmitted signals. The first four IMFs and ignore the extremely low-frequency components are extracted firstly, and the central frequency (CF) of each IMF component can be calculated by the Fast Fourier Transform (FFT). The original waveforms and corresponding IMFs of the models with different fracture porosities (Fig. 8) indicate strong influences of fractures on the attenuation of the wave energy: As the porosity increases, the energy of the original signal decreases. As the IMF increases, the CF range also gradually decreases. The fracture porosity has a more significant effect on the attenuation of IMF1 component, compared with a small decrease in energy of the low-frequency information (IMF3 and IMF4 components), which suggests that the high-frequency information is more sensitive to the fractures.

To analyze the spectral characteristics further, the marginal spectrum – a relationship between energy amplitudes and frequency is applied to offer a higher frequency resolution than the Fourier spectrum. Fig. 9a shows the marginal spectra calculated from the first four IMFs presented in Fig. 8. The CF is 30–40 kHz, which is also the primary energy attenuation range (see the grey shadow, Fig. 9b). The cumulative energy (CE) of the high porosity model A#3.0 is only 23% of the low porosity model A#0.6.

3.2. *Effect of fracture aspect ratio*

Fracture AR has a remarkable effect on elastic wave propagation (Shao and Pyrak-Nolte, 2016), which significantly impacts the energy exchange between the formation and pore fluids. Recent researches only focused on building qualitative trends in velocity and pore type at the core scale (Weger et al., 2009). Alternatively, EMT models can estimate the effective elastic moduli and velocities of carbonate rocks with a complex pore structure by assuming different ARs (Berryman, 1995; Xu and Payne, 2009). However, it is difficult to retrieve

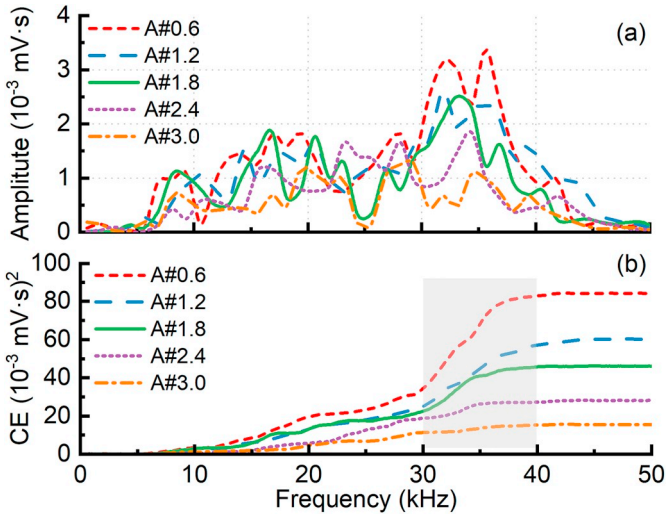

Fig. 9. Marginal spectra of (a) the first four IMFs and (b) the corresponding cumulative energy in the model set A. The attenuation of energy in the frequency domain increases with fracture porosity. The main attenuation range is highlighted in grey.

information about the fracture shape other than porosity via conventional sonic logging (Li et al., 2018). The borehole models of set B have the same fracture size (d = 30 mm) and porosity (1.2%) of set A but different ARs (from 0.017 to 0.13).

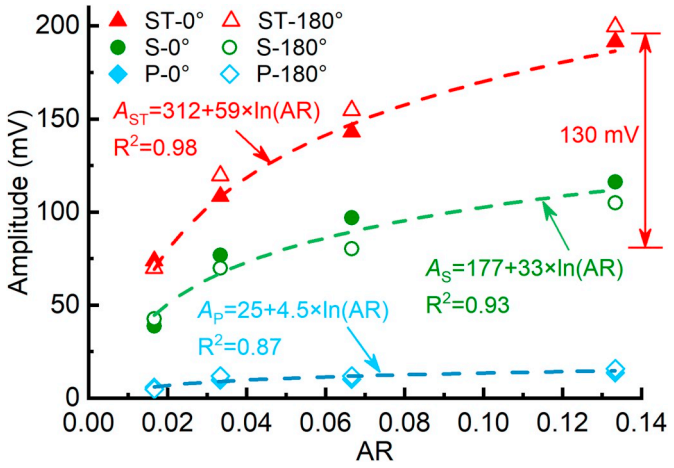

Fig. 11. The relationship between AR and the amplitudes of P-, S-, and Stoneley waves. The corresponding lines are fitted by logarithmic functions for the amplitudes of each wave phase.

The cross-plot between the velocities of the three wave phases and ARs (Fig. 10) shows that the velocities in two directions (0° and 180°) are relatively consistent. The fracture ARs seem to have minimal effects on V_{ST}. However, AR can influence V_P and V_S, especially when the fractures are narrow (AR < 0.1). The relationship between these two parameters generally follows a power law where the determinant coefficients (R^2 value) are as high as 0.9. This higher value and the

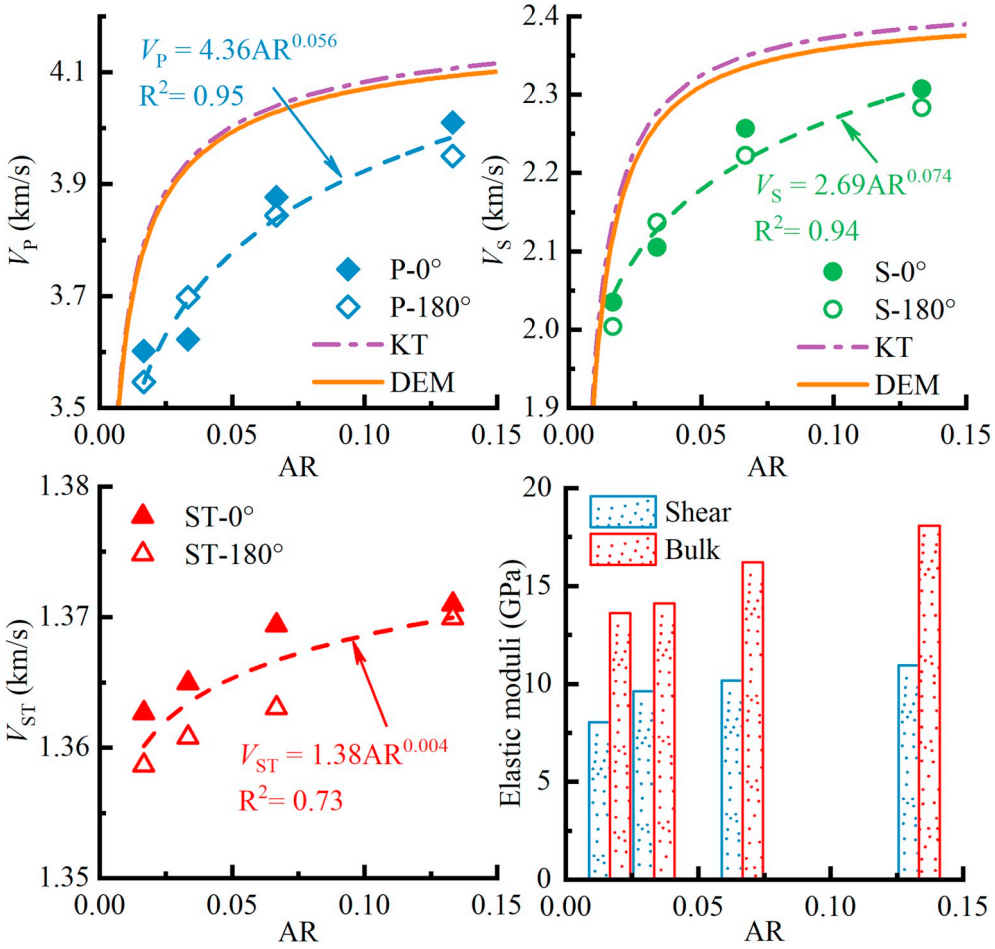

Fig. 10. Influence of the AR on the velocities and elastic moduli for the model set B. The corresponding lines are fitted by a simple power function for the velocities of each wave phase. The fracture porosity (ϕ = 1.2%), size (d = 30 mm), and the source frequency of these models are constant. Two EMT models (KT and DEM) are used to compare with the experimental results.

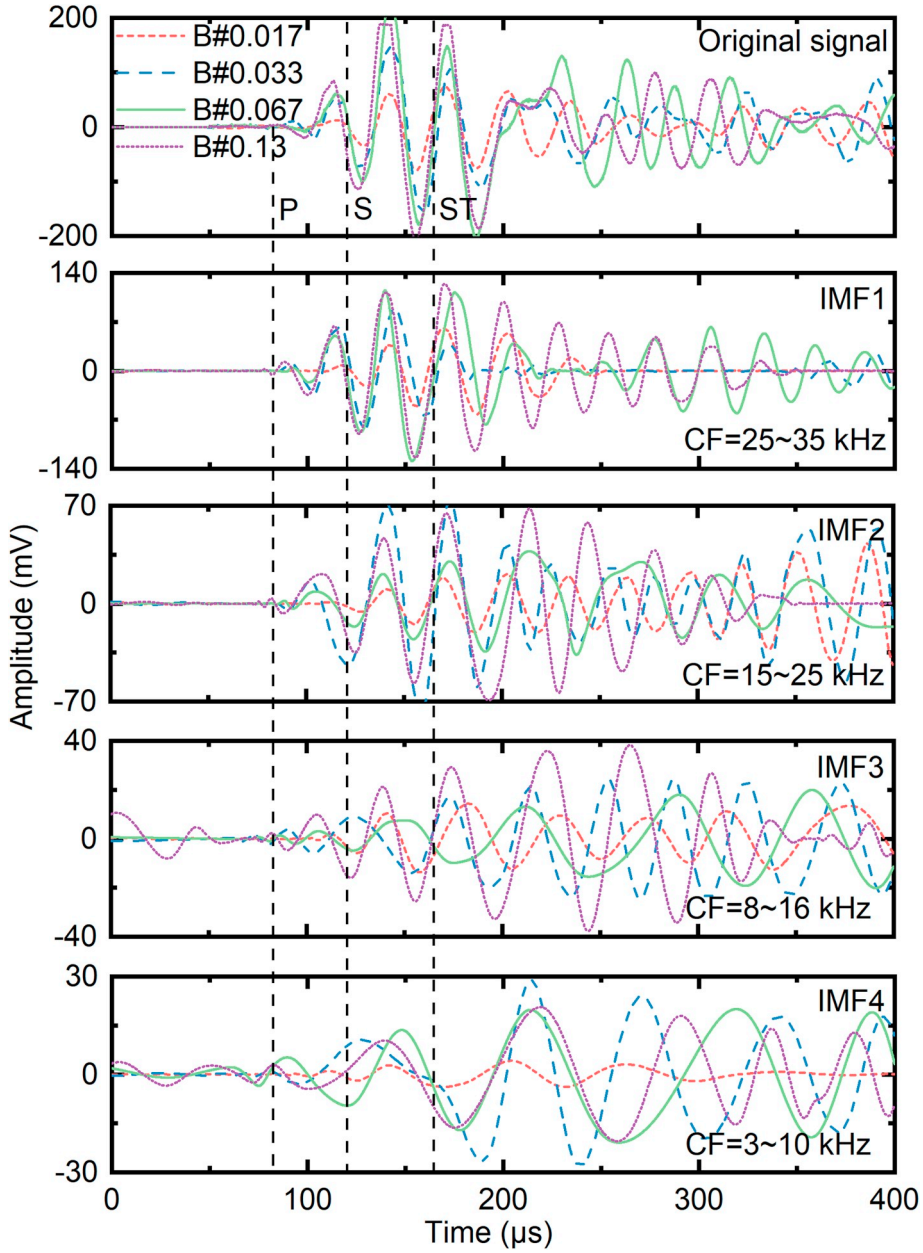

Fig. 12. The original signals received by R1 and the corresponding IMF components in the model set B. The first arrivals of P-, S-, and Stoneley waves in B#0.13 model are indicated by the vertical dashed lines that mark the first breaks of each phase.

stronger sensitivities of V_P, V_S to fracture ARs in KT and DEM models shows that it is inappropriate to directly apply the EMT models at the well-logging scale, especially in the range of low ARs. Compared with the effect of AR in theoretical or experimental models at high frequencies (Li et al., 2016; Wang et al., 2017), relatively small variations of wave velocities are observed at the well-logging scale. The fracture AR has only minor effects on the reflectivity of Stoneley wave, which is frequently targeted by logging analyses due to its sensitivity to fracture aperture and extent (Tang and Cheng, 1993). Considering the complex logging environment, the modest level of variations is easily accommodated by other factors, such as the variation of lithology and hole caliper. Therefore, when the porosity is low, it is difficult to analyze the AR directly from wave velocities alone accurately.

The amplitudes of the three wave phases under different ARs (Fig. 11) reflect the strong effects of the attenuation. The amplitude reduction of the Stoneley wave is 130 mV, which translates to 65% (from 200 mV to 70 mV). The best-fit logarithmic functions positively link the amplitudes of the three waves to fracture ARs, and the overall trends suggest that slimmer fractures can 1) cause more attenuation than the voids or holes with AR > 0.1 and 2) the sensitivity of reflectivity to AR decreases, which is consistent with findings from earlier rock-physical experiments (Li et al., 2016; Wang et al., 2015a,b). This is because increases of ARs results in fewer numbers of fractures under the same porosity, which translates to less solid-fluid interfaces, hence less scattering attenuation (Sevostianov and Kachanov, 2011), along the path of wave propagation.

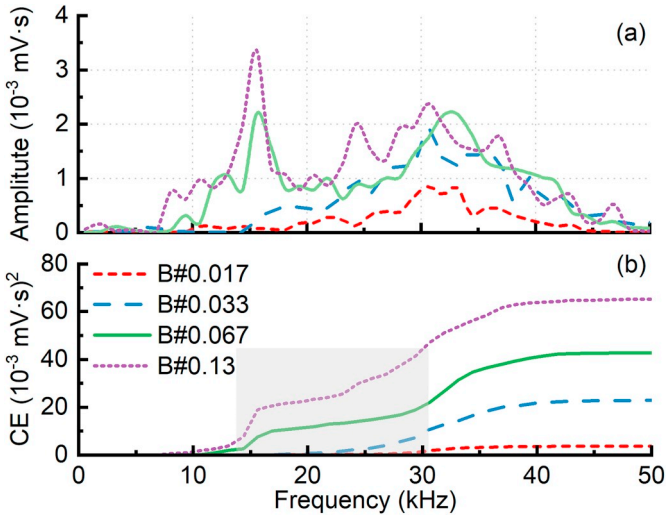

Fig. 13. Marginal spectra of (a) the first four IMFs and (b) the corresponding cumulative energy of model set B. The attenuation of energy in the frequency domain decreases with the fracture AR. The main attenuation range is highlighted in grey.

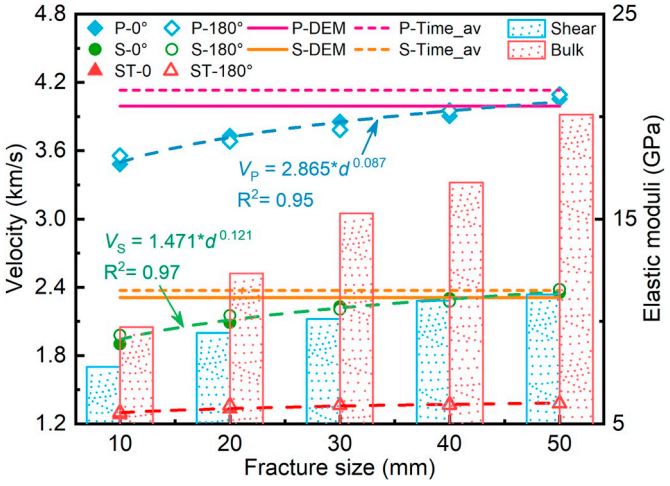

Fig. 14. Influence of fracture size on the velocities and elastic moduli for the model set C. The colors of the best-fit lines using power functions correspond to the velocities of each wave phase. The fracture porosity (ϕ = 1.2%), AR (0.05), and source frequency in these models are constant. DEM model and time average model are used to compare with the experimental results. (For interpretation of the references to color in this figure legend, the reader is referred to the Web version of this article.)

Fig. 12 shows the original waveforms and the corresponding IMFs of the model set B. Although the effect of AR on the attenuation of wave energy is significant, it is difficult to pick the first breaks of the P-, S- and Stoneley waves in the original waveforms (see Fig. 12, first column). The entire intermediate frequency range (15–35 kHz) shows a similar degree of attenuation on the CE (Fig. 13), as suggested by the constant porosity of the models. In other words, scattering attenuation caused by the increased number of solid-fluid interfaces plays a role in a broad frequency range during this experiment.

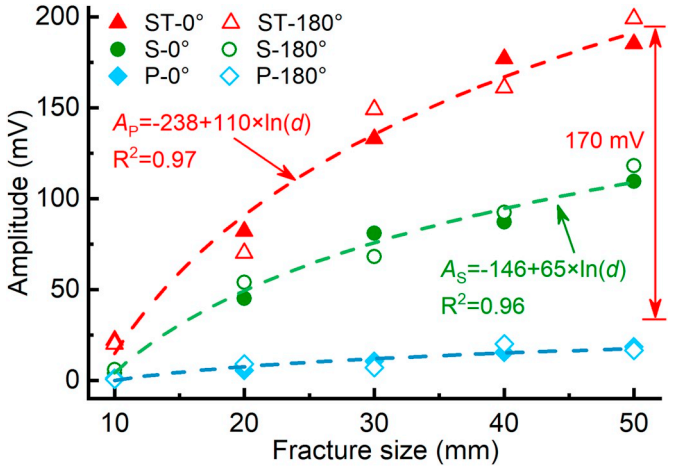

Fig. 15. The relationship between fracture size and the amplitudes of P-, S-, and Stoneley waves. The R^2 values of the logarithmic function are more stable in the case of the Stoneley wave, showing a greater decline of amplitudes than the other wave phases.

3.3. Effect of fracture size

Carbonate rocks usually exhibit a wide range of fracture sizes (Choquette L. C. 1970; Lucia, 1983). The fracture size (d) relative to the wavelength (λ) affects the waveforms of the composite, which has been separated by ray medium ($\lambda < d$) (Cerveny and Brown, 2003), transition medium ($\lambda \approx d$) (Liu and Schmitt, 2006), and effective medium ($\lambda > d$) (Ivankina et al., 2017; Mavko and Nur, 1978). In this experiment, the dominant frequency of the acoustic logging system is 20–40 kHz, and the wavelength is 50–100 mm.

A material with only a few large fractures can have the same fracture porosity as one with many small fractures, an essential factor for the investigation of seismic anisotropy using shear-wave splitting observations from carbonate reservoirs (Maultzsch et al., 2003; Van Der Kolk et al., 2001). The borehole models of set C have the same AR (0.05) and porosity (1%) but different fracture sizes (d = 10–50 mm). Hence, more fractures are required to produce the same porosity when the average fracture size is low. A similar power function also governs the relationship between the wave velocities and fracture sizes, which means a similar mechanism caused by fracture ARs changes can also affect the number of solid-fluid interfaces. The larger indexes used in the power functions in Fig. 14 imply that d has a more significant impact on the velocities, especially of the P-wave. Furthermore, the total porosity calculated by Equation (1) shows a greater dependence on d than on AR. Since the DEM model can provide closer velocities than KT as demonstrated earlier, the DEM model and time average model are adopted to compare with the experimental results. Although these models do not sufficiently describe the effect of fracture size, the DEM model is a valid option when the fracture size is relatively large (i.e., $\lambda \approx d$). Strong dependence on fracture size is further evidenced by a severe reduction of the Stoneley wave amplitude (from 192 mV to 21 mV) (Fig. 15), though signal-to-noise ratio (S/R) of the models with a small fracture size may be a complicating factor.

The first four IMF components of the model set C are shown in Fig. 16. A large number of fractures used in model C#10 result in a higher scattering attenuation as well as a complex waveform with low S/R. The fracture size of model C#50 (50 mm) is close to the wavelength (50–100 mm). When the wave-fronts pass through large fractures, more reflections and refractions (in comparison with smaller fractures) occur according to the Snell's law. The fracture size of model

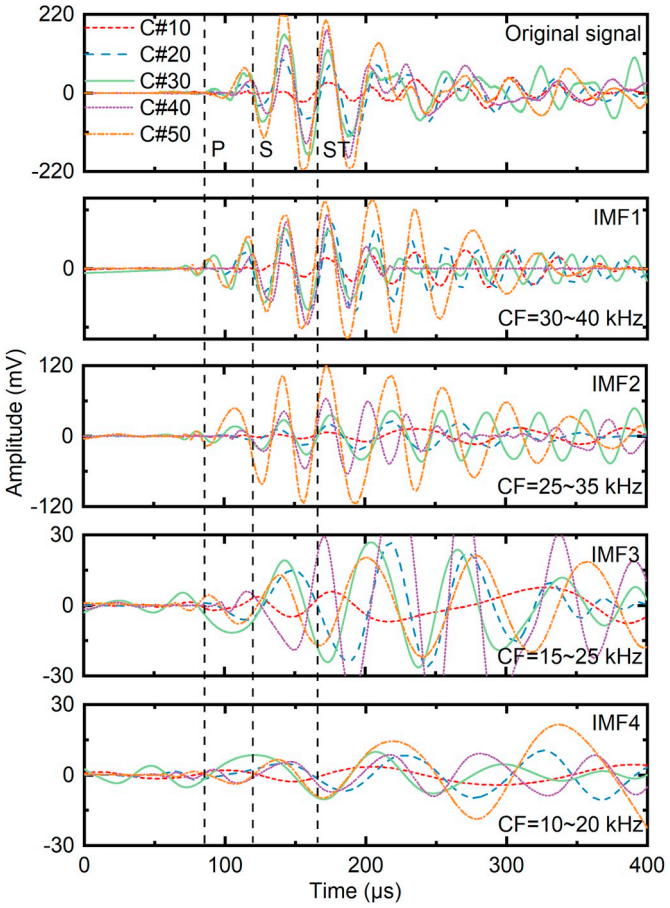

Fig. 16. The original signals received by R1 and the corresponding IMF components in different fracture size models. The first arrivals of P, S and Stoneley waves of the C#50 model are labeled by the vertical dashed lines that mark the first breaks of each wave phase.

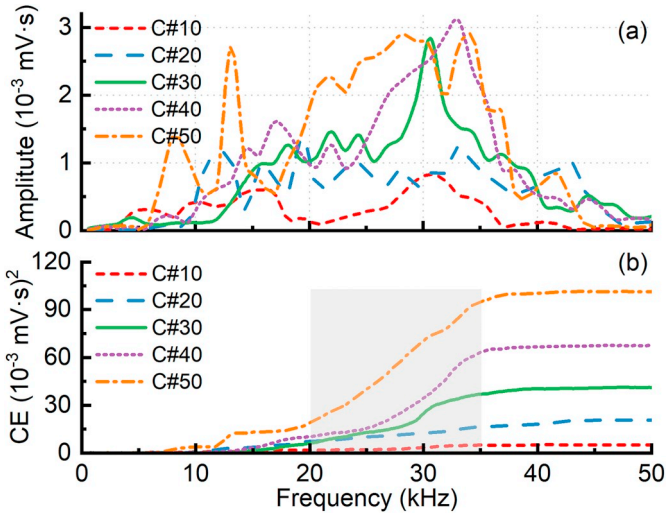

Fig. 17. Marginal spectra of (a) the first four IMFs and (b) the corresponding cumulative energy of model set C. The attenuation of energy in the frequency domain decreases with fracture size. The main attenuation range is highlighted in grey.

C#10 is much smaller than the wavelength and causes more scattering attenuation at the high frequencies (Mavko et al., 2009). Consequently, more peaks are observed in both the original waveform and the IMF components with higher-frequency information than other models with smaller-sized fractures. These time-domain observations are further supported by the marginal spectra (Fig. 17), which shows gradually increasing attenuation from 20 kHz to 40 kHz.

Besides the usefulness of the above results in acoustic logging interpretations, information of the effect of fracture networks on seismic waves is critical for monitoring hydraulic fracturing operations. The experimental results demonstrate that it is feasible to qualitatively evaluate the complexity of fractures, which is more important for predicting their genesis and geometry based on microseismicity or acoustic emissions. However, at low frequencies, the microcracks are much smaller than the wavelength and are, in general, not a key factor for velocity and attenuation. The reduced effect of fracture networks (in comparison with that at high frequencies) may be more evident at microseismic frequencies. Rocks with low fracture ARs and sizes still experience lower velocities and higher attenuation. Therefore, the influence of fractures should not be ignored when interpreting reflection microseismic data of carbonate reservoirs containing complex fracture networks. It is worth reiterating that these results are based on ideal models with isolated penny-shaped fractures. A key characteristic of this model is that it provides only the endmember scenario of saturated, but isolated, fractures, which does not allow for fluid motion between the fracture networks. This is true in the high-frequency limit. Still, the borehole model shown here does provide insight into the influence of fracture structures at lower frequencies compared to the conventional rock-physical models.

4. Conclusions

Existing methods of well-logging interpretation of carbonate reservoirs can be erroneous due to different fracture structures. A new method of devising borehole models with controlled fracture structures is proposed. The modeling results indicate that the conventional rock physics models, such as time average, KT, and DEM, always overestimate the velocities at the well-logging scale. Fracture porosity, AR, and size are all critical factors for acoustic logging, and together they can sufficiently explain variations of velocities and amplitudes in wave propagation. The preparation technology of matrix (cements, carbonate cuttings, and micro-silicon) and fracture distribution, which differ from the existing artificial core methods, are more suitable than conventional approaches for large-scale experiments pertaining to well consolidation and stable properties (e.g., borehole drilling and hydraulic fracturing operations). By analyzing the waveforms in both the time and frequency domains with the HHT method, the results show that the velocity of the Stoneley wave is less sensitive to fracture structures than that of the P- and S-waves, while a relatively significant effect can be observed on the attenuation on the Stoneley wave. As the AR increases, the attenuation becomes more insensitive, which indicates that slimmer fractures can cause more attenuation than voids or holes. Fracture AR and size have a similar attenuation mechanism of increasing the number of solid-fluid interfaces along the wave-propagation paths. The relationships between the properties (velocity and amplitude) and fracture structures (AR and size) conform to power and logarithmic functions, respectively. Compared with absorption attenuation caused by fracture porosities, variations of scattering attenuation at the same porosity are predominantly caused by fracture AR and size. The results have better implications than the rock-physical models for reservoir evaluations and predictions using acoustic logging or microseismic data at lower frequencies.

Acknowledgments

This work was jointly funded by the National Natural Science Foundation of China (Grant No. 51704309 and 51874342), the Fundamental Research Funds for the Central Universities (No. 18CX07008A), and the Future Energy Systems at the University of Alberta.

Appendix A

To solve the problem of the non-linear and non-stationary character of the acoustic logging signal (Li, 2003), we investigate the effect of fractures on acoustic logging signals in the time and frequency domains by the Hilbert-Huang transform (HHT) (Huang et al., 2008, 2003). First, intrinsic mode functions (IMFs) are extracted from the signal based on empirical mode decomposition (EMD). Second, the Hilbert transform is applied to each IMF component to obtain the instantaneous frequency and energy distribution.

The EMD method is used to decompose the original signal into a family of IMF components. The continuous procedure of extracting IMFs is called sifting and is applied as follows.

1. Identify all the local extrema of the original signal $s(t)$. Connect the local maxima and local minima by a cubic spine line as the upper $s_{\max}(t)$ envelope and lower envelope $s_{\min}(t)$.
2. The mean value of the upper and lower envelopes, which covers all the data between them, is m_1. The difference between the data and m_1 is the first component $h_1(t)$.

$$h_1(t) = s(t) - m_1(t) \tag{A-1}$$

3. $h_1(t)$ is treated as a new original signal, and we iterate the above procedure k times until the mean envelope is close to zero. The first IMF component $x_1(t)$ can be designated as:

$$x_1(t) = h_{1(k-1)}(t) = h_{1(k-1)}(t) - m_{1(k-1)}(t) \tag{A-2}$$

where k-1 represents the previous iteration.

4. The residual $r_1(t)$ between the original signal $s(t)$ and $x_1(t)$ is treated as the new input data. Repeat the above procedure until residual $r_j(t)$ becomes a monotonic function from which no more IMFs can be extracted. Each IMF contains lower frequency components than the former one. From the above equations, the original signal $s(t)$ after EMD processing can be expressed as:

$$s(t) = \sum_{i=1}^{n} x_i(t) + r_n(t) \tag{A-3}$$

where $x_i(t)$ are the IMF components and $r_n(t)$ is the stationary residue.

After EMD processing, the complex transmitted signal can be expressed as several IMFs and a stationary residual. The Hilbert transform is applied for each IMF $x_i(t)$ to obtain the instantaneous amplitude, instantaneous phase, and instantaneous frequency. The Hilbert transform function can be described as:

$$y_i(t) = \frac{1}{\pi}\int_{-\infty}^{+\infty} \frac{x_i(\tau)}{t-\tau} d\tau \tag{A-4}$$

With the Hilbert transform $y(t)$ of the function $x(t)$, the analytic function can be obtained by:

$$z_i(t) = x_i(t) + iy_i(t) = A_i(t)e^{i\theta t} \tag{A-5}$$

$$A_i(t) = [x_i^2(t) + y_i^2(t)]^{1/2} \tag{A-6}$$

$$\theta_i(t) = \tan^{-1}\frac{y_i(t)}{x_i(t)} \tag{A-7}$$

where $A(t)$ is the instantaneous amplitude, and $\theta(t)$ is the instantaneous phase function. The instantaneous frequency is expressed as:

$$\omega_i(t) = \frac{d\theta_i(t)}{dt} \tag{A-8}$$

After performing the Hilbert transform on each IMF component and ignoring the residue, the original signal can be expressed as the real part, Re, in the following form:

$$s(t) = \mathrm{Re}\sum_{i=1}^{n} A_i(t)\exp(j\omega(t)dt) \tag{A-9}$$

where $\omega_i(t)$ and $A_i(t)$ are the amplitude and frequency of each component as functions of time, which constitute the three-dimensional time-frequency spectrum in time-energy-frequency space $H(\omega,t)$ as the Hilbert spectrum. Integrating $H(\omega,t)$ over the entire time domain gives the marginal spectrum $h(\omega)$, which is a statistical accumulation of the total magnitude for each frequency:

$$h(\omega) = \int_0^T H(\omega, t)dt \tag{A-10}$$

References

Amalokwu, K., Best, A.I., Chapman, M., 2016. Effects of aligned fractures on the response of velocity and attenuation ratios to water saturation variation: a laboratory study using synthetic sandstones. Geophys. Prospect. 64, 942–957. https://doi.org/10.1111/1365-2478.12378.

Asoodeh, M., Bagheripour, P., 2012. Prediction of compressional, shear, and Stoneley wave velocities from conventional well log data using a committee machine with intelligent systems. Rock Mech. Rock Eng. 45, 45–63. https://doi.org/10.1007/s00603-011-0181-2.

Berryman, J.G., 1992. Single-scattering approximations for coefficients in Biots equations of poroelasticity. J. Acoust. Soc. Am. 91, 551–571. https://doi.org/10.1121/1.402518.

Berryman, J.G., 1995. Mixture Theory for Rock Properties. AGU Handbook of Physical Constants, pp. 205–228. https://doi.org/10.1029/RF003p0205.

Blum, T.E., Snieder, R., Van Wijk, K., Willis, M.E., 2011. Theory and laboratory experiments of elastic wave scattering by dry planar fractures. J. Geophys. Res.: Solid Earth 116, 1–42. https://doi.org/10.1029/2011JB008295.

Bowman, D.C., Lees, J.M., 2013. The Hilbert-Huang transform: a high resolution spectral method for nonlinear and nonstationary time series. Seismol. Res. Lett. 84, 1074–1080. https://doi.org/10.1785/0220130025.

Cerveny, V., Brown, M.G., 2003. Seismic Ray Theory, the Journal of the Acoustical Society of America. Cambridge university press. https://doi.org/10.1121/1.1523385.

Choquette, P.W., Pray, L.C., 1970. Geologic nomenclature and classification of porosity in sedimentary carbonates. AAPG (Am. Assoc. Pet. Geol.) Bull. 54, 207–250. https://doi.org/10.1306/5D25C98B-16C1-11D7-8645000102C1865D.

Crampin, S., Gao, Y., Bukits, J., 2015. A review of retrospective stress-forecasts of earthquakes and eruptions. Phys. Earth Planet. Inter. 245, 76–87. https://doi.org/10.1016/J.PEPI.2015.05.008.

De Figueiredo, J.J.S., Schleicher, J., Stewart, R.R., Dayur, N., Omoboya, B., Wiley, R., William, A., 2013. Shear wave anisotropy from aligned inclusions: ultrasonic frequency dependence of velocity and attenuation. Geophys. J. Int. 193, 475–488. https://doi.org/10.1093/gji/ggs130.

Du, J., Bu, Y., Shen, Z., Cao, X., 2019. A novel fluid for use in oil and gas well construction to prevent the oil and gas leak from the wellbore. Constr. Build. Mater. 217, 626–637. https://doi.org/10.1016/J.CONBUILDMAT.2019.05.100.

Fan, G., Zhang, L.M., Zhang, J.J., Ouyang, F., 2017. Energy-based analysis of mechanisms of earthquake-induced landslide using Hilbert–Huang transform and marginal spectrum. Rock Mech. Rock Eng. 50, 2425–2441. https://doi.org/10.1007/s00603-017-1245-8.

Flügel, E., 2004. Microfacies of Carbonate Rocks: Analysis, Interpretation and Application. Springer Science & Business Media.

Guo, J., Germán Rubino, J., Barbosa, N.D., Glubokovskikh, S., Gurevich, B., 2018. Seismic dispersion and attenuation in saturated porous rocks with aligned fractures of finite thickness: theory and numerical simulations — Part 2: frequency-dependent anisotropy. Geophysics 83, WA63–WA71. https://doi.org/10.1190/geo2017-0066.1.

Haach, V.G., Vasconcelos, G., Loureno, P.B., 2011. Influence of aggregates grading and water/cement ratio in workability and hardened properties of mortars. Constr. Build. Mater. 25, 2980–2987. https://doi.org/10.1016/j.conbuildmat.2010.11.011.

Han, D., Nur, A., Morgan, D., 1986. Effects of porosity and clay content on wave velocities in sandstones. Geophysics 51, 2093–2107. https://doi.org/10.1190/1.1442062.

Hornby, B.E., Johnson, D.L., Winkler, K.W., Plumb, R.A., 1989. Fracture evaluation using reflected Stoneley-wave arrivals. Geophysics 54, 1274–1288.

Huang, N.E., Wu, M.L., Qu, W., Long, S.R., Shen, S.S.P., 2003. Applications of Hilbert–Huang transform to non-stationary financial time series analysis. Appl. Stoch Model Bus. Ind. 19, 245–268.

Huang, N.E., Wu, Z., others, 2008. A review on Hilbert-Huang transform: method and its applications to geophysical studies. Rev. Geophys. 46, 1–23. https://doi.org/10.1029/2007RG000228.

Ivankina, T.I., Zel, I.Y., Lokajicek, T., Kern, H., Lobanov, K.V., Zharikov, A.V., 2017. Elastic anisotropy of layered rocks: ultrasonic measurements of plagioclase-biotite-muscovite (sillimanite) gneiss versus texture-based theoretical predictions (effective media modeling). Tectonophysics 712–713, 82–94. https://doi.org/10.1016/j.tecto.2017.05.005.

Jeppson, T.N., Tobin, H.J., 2015. San Andreas fault zone velocity structure at SAFOD at core, log, and seismic scales. J. Geophys. Res.: Solid Earth 120, 4983–4997. https://doi.org/10.1002/2015JB012043.

Johnston, D.H., Toksöz, M.N., Timur, A., 1979. Attenuation of seismic waves in dry and saturated rocks: II. mechanisms. Geophysics 44, 691–711. https://doi.org/10.1190/1.1440970.

Kuster, G.T., Toksöz, M.N., 1974. Velocity and attenuation of seismic waves in two-phase media: Part Ii. Experimental results. Geophysics 39, 607–618. https://doi.org/10.1190/1.1440451.

Leary, P.C., Crampin, S., McEvilly, T.V., 1990. Seismic fracture anisotropy in the Earth's crust: an overview. J. Geophys. Res. 95, 11105. https://doi.org/10.1029/JB095iB07p11105.

Li, C.F., 2003. Rescaled-range and power spectrum analyses on well-logging data. Geophys. J. Int. 153, 201–212. https://doi.org/10.1046/j.1365-246X.2003.01893.x.

Li, T., Wang, R., Wang, Z., Wang, Y., 2016. Experimental study on the effects of fractures on elastic wave propagation in synthetic layered rocks. Geophysics 81, D441–D451. https://doi.org/10.1190/geo2015-0661.1.

Li, T., Wang, R., Wang, Z., Zhao, M., Li, L., 2018. Prediction of fracture density using genetic algorithm support vector machine based on acoustic logging data. Geophysics 83. https://doi.org/10.1190/GEO2017-0229.1.

Li, T., Gu, Y.J., Wang, Z., Wang, Ruijia, Chen, Y., Song, T.A., Wang, Ruihe, 2019a. Spatiotemporal variations in crustal seismic anisotropy surrounding induced earthquakes near Fox creek, Alberta. Geophys. Res. Lett. 46, 5180–5189. https://doi.org/10.1029/2018GL081766.

Li, T., Wang, R., Wang, Z., 2019b. A method of rough pore surface model and application in elastic wave propagation. Appl. Acoust. 143, 100–111. https://doi.org/10.1016/J.APACOUST.2018.08.031.

Liu, Y., Schmitt, D.R., 2006. The transition between the scale domains of ray and effective medium theory and anisotropy: numerical models. Pure Appl. Geophys. 163, 1327–1349. https://doi.org/10.1007/s00024-006-0075-5.

Liu, J., Pereira, G.G., Liu, Q., Regenauer-Lieb, K., 2016. Computational challenges in the analyses of petrophysics using microtomography and upscaling: a review. Comput. Geosci. 89, 107–117. https://doi.org/10.1016/J.CAGEO.2016.01.014.

Lucia, F.J., 1983. Petrophysical parameters estimated from visual descriptions of carbonate rocks: a field classification of carbonate pore space. J. Pet. Technol. 35, 629–637. https://doi.org/10.2118/10073-PA.

Maultzsch, S., Chapman, M., Liu, E., Li, X.Y., 2003. Modelling frequency-dependent seismic anisotropy in fluid-saturated rock with aligned fractures: implication of fracture size estimation from anisotropic measurements. Geophys. Prospect. 51, 381–392. https://doi.org/10.1046/j.1365-2478.2003.00386.x.

Mavko, G.M., Nur, A., 1978. The effect of nonelliptical cracks on the compressibility of rocks. J. Geophys. Res. Solid Earth 83, 4459–4468.

Mavko, G., Mukerji, T., Dvorkin, J., 2009. The Rock Physics Handbook Tools for Seismic Analysis of Porous Media. Cambridge university press. https://doi.org/10.1029/2007JD009719.

Maxwell, S.C., Bennett, L., Jones, M., Walsh, J., 2010. Anisotropic velocity modeling for microseismic processing: Part 1—impact of velocity model uncertainty. In: SEG Technical Program Expanded Abstracts 2010, pp. 2130–2134. https://doi.org/10.1190/1.3513267.

Mehrabi, H., Mansouri, M., Rahimpour-Bonab, H., Tavakoli, V., Hassanzadeh, M., 2016. Chemical compaction features as potential barriers in the Permian-Triassic reservoirs of Southern Iran. J. Pet. Sci. Eng. 145, 95–113. https://doi.org/10.1016/j.petrol.2016.03.020.

Meng, M., Zamanipour, Z., Miska, S., Yu, M., Ozbayoglu, E.M., 2019. Dynamic stress distribution around the wellbore influenced by surge/swab pressure. J. Pet. Sci. Eng. 172, 1077–1091. https://doi.org/10.1016/J.PETROL.2018.09.016.

Pan, X., Zhang, G., Yin, X., 2018. Elastic impedance variation with angle and azimuth inversion for brittleness and fracture parameters in anisotropic elastic media. Surv. Geophys. 39, 965–992. https://doi.org/10.1007/s10712-018-9491-1.

Rahimpour-Bonab, H., Mehrabi, H., Enayati-Bidgoli, A.H., Omidvar, M., 2012a. Coupled imprints of tropical climate and recurring emergence on reservoir evolution of a mid Cretaceous carbonate ramp, Zagros Basin, southwest Iran. Cretac. Res. 37, 15–34. https://doi.org/10.1016/j.cretres.2012.02.012.

Rahimpour-Bonab, H., Mehrabi, H., Navidtalab, A., Izadi-Mazidi, E., 2012b. Flow unit distribution and reservoir modelling in cretaceous carbonates of the sarvak formation, Abteymour oilfield, dezful embayment, SW Iran. J. Pet. Geol. 35, 213–236. https://doi.org/10.1111/j.1747-5457.2012.00527.x.

Sarmadivaleh, M., Rasouli, V., 2014. Test design and sample preparation procedure for experimental investigation of hydraulic fracturing interaction modes. Rock Mech. Rock Eng. 48, 93–105. https://doi.org/10.1007/s00603-013-0543-z.

Schmitt, D.R., 2015. Geophysical properties of the near surface earth: seismic properties. In: Treatise on Geophysics, second ed. Elsevier, pp. 43–87. https://doi.org/10.1016/B978-0-444-53802-4.00190-1.

Sevostianov, I., Kachanov, M., 2011. Elastic fields generated by inhomogeneities: far-field asymptotics, its shape dependence and relation to the effective elastic properties. Int. J. Solids Struct. 48, 2340–2348. https://doi.org/10.1016/j.ijsolstr.2011.04.014.

Shalaby, M.R., Islam, M.A., 2017. Fracture detection using conventional well logging in carbonate Matulla Formation, Geisum oil field, southern Gulf of Suez, Egypt. J. Pet. Explor. Prod. Technol. 7, 977–989. https://doi.org/10.1007/s13202-017-0343-1.

Shao, S., Pyrak-Nolte, L.J., 2016. Wave propagation in isotropic media with two orthogonal fracture sets. Rock Mech. Rock Eng. 49, 4033–4048. https://doi.org/10.1007/s00603-016-1084-z.

Shuai, D., Wei, J., Di, B., Yuan, S., Xie, J., Yan, S., 2018. Experimental study of fracture size effect on elastic-wave velocity dispersion and anisotropy. Geophysics 83, C49–C59. https://doi.org/10.1190/geo2016-0639.1.

Spies, B.R., 1996. Electrical and electromagnetic borehole measurements: a review. Surv. Geophys. 17, 517–556. https://doi.org/10.1007/BF01901643.

Tang, X.M., Cheng, C.H., 1993. Borehole Stoneley wave propagation across permeable structures. Geophys. Prospect. 41, 165–187. https://doi.org/10.1111/j.1365-2478.1993.tb00864.x.

Tillotson, P., Sothcott, J., Best, A.I., Chapman, M., Li, X.Y., 2012. Experimental verification of the fracture density and shear-wave splitting relationship using synthetic silica cemented sandstones with a controlled fracture geometry. Geophys. Prospect. 60, 516–525. https://doi.org/10.1111/j.1365-2478.2011.01021.x.

Van Der Kolk, C.M., Guest, W.S., Potters, J.H.H.M., 2001. The 3D shear experiment over the Natih field in Oman: the effect of fracture-filling fluids on shear propagation. Geophys. Prospect. 49, 179–197. https://doi.org/10.1046/j.1365-2478.2001.00250.x.

Wang, Z., Wang, R., Li, T., Qiu, H., Wang, F., 2015. Pore-scale modeling of pore structure effects on P-wave scattering attenuation in dry rocks. PLoS One 10. https://doi.org/10.1371/journal.pone.0126941.

Wang, Z., Wang, R., Wang, F., Qiu, H., Li, T., 2015b. Experiment study of pore structure effects on velocities in synthetic carbonate rocks. Geophysics 80. https://doi.org/10.1190/GEO2014-0366.1.

Wang, Z., Schmitt, D.R., Wang, R., 2017. Modeling of viscoelastic properties of non-permeable porous rocks saturated with highly viscous fluid at seismic frequencies at

the core scale. J. Geophys. Res.: Solid Earth 122, 6067–6086. https://doi.org/10.1002/2017JB013979.

Weger, R.J., Eberli, G.P., Baechle, G.T., Massaferro, J.L., Sun, Y.F., 2009. Quantification of pore structure and its effect on sonic velocity and permeability in carbonates. AAPG (Am. Assoc. Pet. Geol.) Bull. 93, 1297–1317. https://doi.org/10.1306/05270909001.

Xu, S., Payne, M.A., 2009. Modeling elastic properties in carbonate rocks. Lead. Edge 28, 66–74. https://doi.org/10.1190/1.3064148.

Yuan, D., Engineering, P., Li, A., Stewart, R., 2016. Joint inversion for anisotropic velocity model and event locations using S-wave splitting measurements from downhole microseismic data. Geophysics 82, 2508–2512. https://doi.org/10.1190/geo2016-0221.1.

Zhou, J., Jin, Y., Chen, M., 2010. Experimental investigation of hydraulic fracturing in random naturally fractured blocks. Int. J. Rock Mech. Min. Sci. 47, 1193–1199. https://doi.org/10.1016/j.ijrmms.2010.07.005.

Zhu, Z., Toksz, M.N., Zhan, X., 2016. Seismoelectric measurements in a porous quartz-sand sample with anisotropic permeability. Geophys. Prospect. 64, 700–713. https://doi.org/10.1111/1365-2478.12304.